Hydrous melts weaken the mantle, crystallization of pargasite and phlogopite does not: Insights from a petrostructural study of the Finero peridotites, southern Alps

Andrea Tommasi, Antonio Langone, Jose Alberto Padron Navarta, Alberto Zanetti, Alain Vauchez

Author copy of the final (peer-reviewed) version of the article published in Earth and Planetary Science Letters
Please, reference to: Tommasi, A., Langone, A., Padron-Navarta, J.A., Zanetti, A., Vauchez, A. Hydrous melts weaken the mantle, crystallization of amphibole and phlogopite does not: Insights from a petrostructural study of the Finero peridotites, southern Alps. Earth Planet. Sci. Lett., 477: 59-72, doi: 10.1016/j.epsl.2017.08.015

Hydrous melts weaken the mantle, crystallization of pargasite and phlogopite does not: Insights from a petrostructural study of the Finero peridotites, southern Alps

Andréa Tommasi [a,*], Antonio Langone [b], José Alberto Padrón-Navarta [a], Alberto Zanetti [b], Alain Vauchez [a]

[a] *Géosciences Montpellier, Univ. Montpellier & CNRS, Montpellier, France*
[b] *Istituto di Geoscienze e Georisorse, C.N.R., Pavia, Italy*

Keywords:
upper mantle rheology
subduction
hydrous melts
strain localization
dissolution–precipitation creep
upper mantle hydration

A B S T R A C T

This study reports petrostructural observations in the pargasite and phlogopite-bearing Finero peridotite massif (Italian Western Alps), which suggest that the pervasive foliation in this massif was formed by deformation concomitant with percolation of hydrous Si-rich melts: (1) diffuse contacts, but systematic parallelism between the pyroxenitic layers and the foliation of the peridotite (2) strong shape and crystal preferred orientations (SPO and CPO), but subhedral or interstitial shapes and weak intracrystalline deformation of the hydrous phases, (3) CPO, but interstitial shapes of the pyroxenes, (4) very coarse olivine grain sizes, which are correlated to the olivine abundance, and (5) elongated shapes, but weak intracrystalline deformation, and extremely weak and highly variable CPO of olivine. The pervasive deformation of the Finero peridotite occurred therefore under conditions that allowed coexistence of H_2O–CO_2-bearing melts, pargasite, and spinel, that is, temperatures of 980–1080 °C and pressures <2 GPa. The petrostructural observations suggest that the presence of hydrous melts results in accommodation of large amounts of deformation by stress-controlled dissolution–precipitation and advective transport of matter by the melts and in fast grain boundary migration in olivine. By consequence, it produces significant rheological weakening. Water contents in olivine are <4 ppm wt., implying limited contribution of hydration of olivine to weakening. In addition, the analysis of protomylonites composing the external domains of the shear zones that overprint the pervasive foliation indicates that the transition to melt-free conditions results in enhanced contribution of dislocation creep to the deformation. The associated increase of the peridotites' strength leads to onset of strain localization. The latter is not correlated to the local abundance in pargasite or phlogopite, implying that crystallization of amphiboles or phlogopite, even at concentrations of 25 vol.%, does not produce rheological weakening in the upper mantle.

1. Introduction

It is commonly accepted that hydration leads to significant weakening in the mantle. However, incorporation of water in the upper mantle results in different processes depending on the pressure and temperature conditions and on the water activity: (i) crystallization of hydrous minerals, (ii) incorporation of different hydrous point defects in the structure of olivine and pyroxenes, (iii) partial melting with partitioning of the water in the melt, or (iv) accumulation (and migration) of aqueous fluids in the peridotites.

Most of the existing experimental data accounting for the effect of water on the rheology has been obtained on the dry-end part of the water–peridotite system. The experiments focused on the rheological effect of hydrogen incorporation in the olivine structure, at conditions under which hydrous minerals are not stable. They corroborate that this hydration process, which occurs at the part per million level of equivalent H_2O, produces weakening, but the data differ on the estimation of its intensity. A first series of experiments suggested an almost linear increase in strain rate at constant stress with increasing hydrous point defect concentration in olivine (Mei and Kohlstedt, 2000a, 2000b). Subsequent diffusion and deformation experiments on single crystals suggested that this

* Corresponding author.
E-mail address: andrea.tommasi@umontpellier.fr (A. Tommasi).

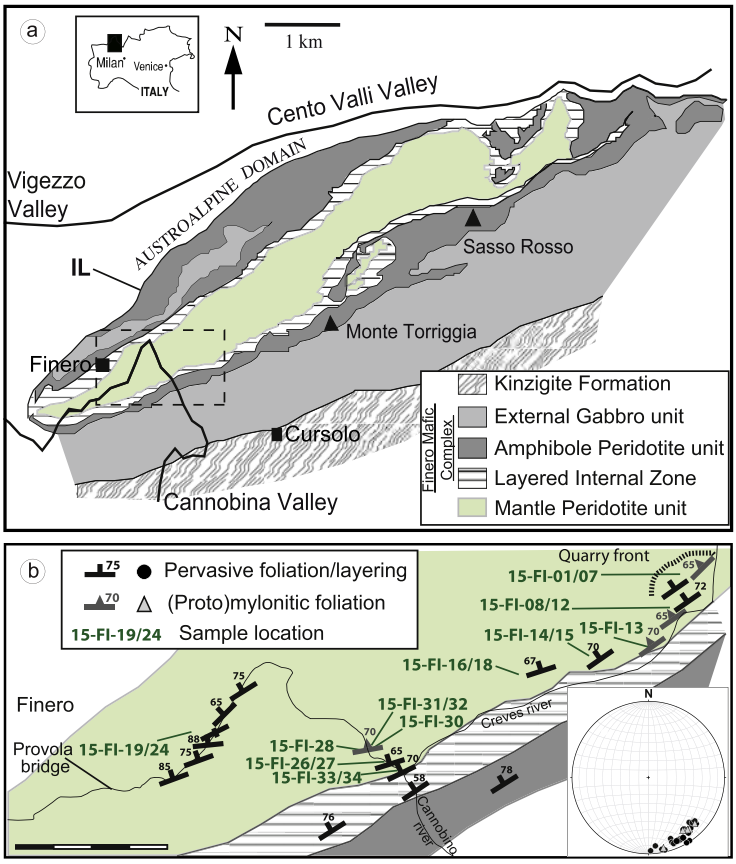

Fig. 1. (a) Sketch map of the northern sector of the Ivrea–Verbano Zone showing the main units of the Finero Complex, as well as the Insubric Line (IL) and the Kinzigite Formation, which bound it to the NW and SE, respectively. (b) Geological map of the area east/northeast of Finero village displaying samples' locations and foliation planes. Insert shows a stereonet (equal-area projection, lower hemisphere) of poles of the main pervasive foliation of the coarse-grained peridotites and of the foliation in the shear zones.

effect was likely overestimated for both diffusion (Fei et al., 2013) and dislocation creep regimes (Girard et al., 2013). The latter experiments show a modest weakening by a factor 1.3–1.6 for water contents of at least 290 H/10^6Si (18 ppm wt. of H_2O) and no significant effect on further incorporation of hydrogen. These results are consistent with torsion experiments on wet olivine polycrystals, which show a modest strength decrease by a factor of 2–3 relative to dry samples associated with hydrous defects in olivine and water-derived species in grain boundaries (Demouchy et al., 2012). Finally, recent data suggest that the weakening might depend on the type of hydrous defect in olivine, claiming for a higher rheological sensitivity to hydrogen when it is coupled to other trace elements, such as titanium (Faul et al., 2016).

There are few data on the mechanical behavior of peridotites in presence of hydrous melts. Comparison between experiments on olivine + basalt and olivine + basalt + water samples indicate that the presence of water in the system results in an increase in strain rate at constant stresses by ~2 orders of magnitude relative to dry systems in both the dislocation and diffusion creep regimes (Mei et al., 2002).

No experimental data constrain the rheological effects of the crystallization of hydrous minerals, such as amphiboles, chlorite, phlogopite, or of the presence of water-rich fluids in a peridotite. Yet, these processes are expected to be the dominant response to hydration in large domains of the mantle wedge and in the lithospheric mantle (e.g., Fumagalli and Klemme, 2015). Observations in natural systems deformed under such conditions are also rare. A recent study of a mantle shear zone in the Ronda peridotite points nevertheless to a major role of pressure-solution on the deformation of mantle rocks in presence of fluids at low temperature and pressure (Hidas et al., 2016).

In summary, the deformation processes and, by consequence, the rheology of the mantle in presence of hydrous melts, fluids, or hydrous minerals, like pargasite and phlogopite, are poorly known. This knowledge is essential for understanding how the base of the upper plate and the moderate temperature domains of the mantle wedge deform and for predicting the coupling between the plates (both subducting and overlying) and the convecting mantle wedge.

Petrostructural and chemical study of the pargasite-phlogopite peridotites of the Finero complex, in the Western Italian Alps, may provide answers to these questions by unraveling:

- Which are the deformation processes active in the mantle in the pargasite and phlogopite stability field, that is, at temperatures below 1080 °C?
- How does the presence of hydrous melts change the deformation processes and the mantle rheology?
- Does enrichment in hydrous phases by itself modify the rheology of a peridotite? May it promote strain localization?

2. Geological setting

The Finero complex is a unique example of a large orogenic mafic–ultramafic massif recording melt percolation leading to pervasive crystallization of large amounts (up to 25 vol.%) of pargasite and phlogopite in peridotites. It outcrops as a lens-shaped body in the northernmost part of the Ivrea–Verbano Zone (Fig. 1a). It is bounded to the N–NW by the Insubric line (IL, Fig. 1a), which places it in contact with an accretionary prism of the Alpine

orogeny, the Sesia–Lanzo Zone, and to the S–SE by the granulite-to-amphibolite facies metapelites and metavolcanics of the polymetamorphic basement (Kinzigite Formation, Fig. 1a) of the Adria plate.

The Mantle Peridotite unit studied here represents the inner portion of the Finero complex (Lensch, 1968). It is wrapped by an intercalation of mafic–ultramafic lithologies, which compose the Finero Mafic Complex: i) the Layered Internal Zone, ii) the Amphibole Peridotite unit, and iii) the External Gabbro unit (Fig. 1a; Cawthorn, 1975; Coltorti and Siena, 1984; Lu et al., 1997; Zanetti et al., 1999, 2013). All units have sub-vertical contacts and internal structures (layering and/or foliation). The present vertical orientation of the structures may result from rotations during the opening of the Jurassic Tethys and the Alpine collision (Rutter et al., 2007; Wolff et al., 2012; Beltrando et al., 2015), but the internal orientation relations have not been affected by these later events.

The Mantle Peridotite unit consists mainly of harzburgite and dunite (usually in lenses) with considerable amounts of pargasite and phlogopite, which are locally associated with cm-thick pyroxenite layers. The latter are very common in the study area (Fig. 1a), but less frequent elsewhere in the massif. Large dunite bodies often display thick layers or massive patches of chromite (Zanetti et al., 2016 and references therein). Chromitites also occur as thin discontinuous layers oblique to the foliation in the smaller dunite bodies.

The Mantle Peridotite unit is usually interpreted as a metasomatized mantle section, in which pervasive to channeled migration of hydrous melts resulted in crystallization of hydrous phases (phlogopite and pargasite) and pyroxenes (Hartmann and Wedepohl, 1993; Zanetti et al., 1999). Phlogopite-bearing bands and pockets were also documented in the Amphibole Peridotite Unit (Giovanardi et al., 2014). The widespread enrichment in orthopyroxene, pargasite, and phlogopite, as well as the trace element and the isotopic compositions of the peridotites and associate pyroxenites were interpreted as indicating interaction with water- and Si-rich melts and, hence, a supra-subduction environment for the metasomatism of the Finero peridotites (e.g., Hartmann and Wedepohl, 1993; Zanetti et al., 1999, 2016; Selverstone and Sharp, 2011).

The whole ultramafic/mafic complex shows evidence for multiple deformation events under decreasing metamorphic conditions. The earliest deformation produced a pervasive foliation. It was followed by the formation of discrete shear zones a few centimeters to meters wide and by brittle faulting (Kruhl and Voll, 1976, 1979; Garuti and Friolo, 1979; Brodie, 1980, 1981; Altenberger, 1995; Kenkmann and Dresen, 2002; Matysiak and Trepmann, 2015).

3. Field observations

Field work and samples collection were performed on newly exposed outcrops from an active quarry front close to the Finero village, along the private road to the quarry, and along the Cannobino river, from the Provola bridge to the Creves–Cannobino confluence, where the contact between the Mantle Peridotite and the Layered Internal Zone is exposed (Fig. 1b).

Harzburgites are the dominant rock type (Fig. 2). They can contain large amounts of pargasite (up to 23 vol.%) or phlogopite (up to 21 vol.%, Table 1). These two phases are distributed pervasively in the peridotite and their alignment marks the foliation, but their contents vary strongly at the cm scale (Fig. 2a).

The harzburgites host mm to tens of cm-wide orthopyroxenite and Cr-diopside websteritic layers (Fig. 2b, c, d), which define a compositional layering parallel to the harzburgite foliation. These pyroxenitic layers have diffuse limits and finite lengths, with lens-shape terminations (Fig. 2c, d). Websteritic layers often have irregular shapes and are enriched in orthopyroxene at the contact with the harzburgites. Orthopyroxenite layers tend to be more planar. A secondary set of orthopyroxenite layers forming conjugate structures at $\sim 20^\circ$ to the set parallel to the foliation is observed locally (Fig. 2b). At the contact with websteritic and orthopyroxenitic layers, the peridotite is usually enriched in olivine and depleted in pargasite. However, in the vicinity of some websterites, the peridotite has a lherzolitic composition.

Dunites occur mainly as tens of centimeters to several meters wide lens-shaped bodies elongated parallel to the harzburgite foliation (Fig. 2e, f). Compared to the harzburgites, the dunites are usually enriched in phlogopite and depleted in pargasite. The contact of the dunites with the harzburgites is always diffuse. They contain mm- to cm-sized chromite-rich seams, which are often oblique to the foliation in the neighboring harzburgites.

Except when affected by shear zones, all lithologies are coarse- to very coarse-grained and display a pervasive steeply dipping foliation. There are variations in dip angle, but in average the foliation is parallel to the contact with the gabbros of the Layered Internal Zone (Fig. 1b) and to the magmatic foliation of the latter. Lineations are difficult to recognize in the field, but the analysis of crystal preferred orientations (cf. section 5) indicate that although the fabric has a strong planar component, it contains a subhorizontal lineation.

Several shear zones with thicknesses ranging from centimeters to a few meters are observed in the quarry and in the Cannobino river outcrops. These shear zones are characterized by a marked grain size reduction, which in some cases leads to the formation of mm- to cm-scale ultramylonite bands. They show an anastomosed structure with, in most cases, a general orientation of the foliation subparallel to the pervasive foliation in the harzburgites (Fig. 1b). Within the shear zones, the pyroxenite layers are usually boudinaged and have sharper contacts with the harzburgites. Some of these shear zones evolve into or are overprinted by brittle faults, characterized by extreme grain size reduction, forming gauges and, locally, pseudotachylites. Brittle structures are usually <10 cm thick. These shear zones have been extensively studied. They result from multiple episodes of deformation under decreasing temperature conditions, probably separated by significant time hiatus (Brodie, 1980, 1981; Altenberger, 1995; Matysiak and Trepmann, 2015). This interpretation is corroborated, in the study area, by the observation of sapphirine-bearing gabbroic veins, which crosscut the pervasive foliation and the foliation of the protomylonites in the external domains of a shear zone, but are deformed in a few cm-wide mylonitic to ultramylonitic band parallel to the protomylonites foliation.

In the present work, we focus on the pervasive deformation of the massif, which predated the formation of shear zones, and on the initial stages of strain localization, that is, on the transition from distributed to localized deformation. The latter is recorded by the protomylonites that compose the external domains of some shear zones.

4. Microstructures

Olivine grain size in the peridotites increases with olivine content (Figs. 3 and 4); dunites are very coarse-grained (5 mm in average, Table 1), whereas pargasite- or phlogopite-rich harzburgites and lherzolites have smaller olivine crystals (1.7 mm in average, Table 1). Olivine in the harzburgites and lherzolites displays a shape-preferred orientation (area-weighted aspect ratios of 2 in average, Table 1), which marks the foliation (Fig. 3a–f). In dunites, in contrast, olivine has polygonal, equiaxed shapes (Fig. 3g, h). Intermediate microstructures characterize the olivine-rich domains in the vicinity of the pyroxenite layers (Figs. 3c–f).

In all lithologies, olivine displays variable densities of intragranular deformation features. In some samples, olivine is almost

Table 1
Samples description, modes, microstructural, and crystal preferred orientation parameters.

Sample								Microstructure								Crystal Preferred Orientation (CPO)					
Name	Lithology	Modal proportions						Grain size[1]				Olivine recrystallization		Aspect ratio		Olivine			OPX	CPX	Pargasite
		Ol	Opx	Cpx	Par	Phl	Spl	Ol	Opx	Cpx	Par	Area fraction	Grain size[2]	Ol	Amph	J-1ppg	BA-1ppg	KAM	J-1ppg	J-1ppg	J-1ppg
15-FI-01	Harzburgite (protomylonite)	77%	15%	1%	3%	3%	1%	1232	562	166	574	0.30	144	2.01	1.89	1.7	0.26	1.20	1.2	4.6	2.6
15-FI-02A	Harzburgite + websterite	36%	27%	32%	5%	0%	<1%	2911	1420	2004	660	0	–	1.97	1.98	2.2	0.44	0.90	2.2	2.8	4.3
15-FI-02B	Harzburgite	76%	15%	4%	4%	<1%	<1%	2106	992	591	847	0	–	2.03	1.66	1.9	0.38	0.73	2.6	4.9	#
15-FI-03	Dunite (protomylonite)	94%	<1%	1%	1%	3%	1%	5627			326	0.13	440	2.09	1.87	2.0	0.13	0.78	#	#	#
15-FI-04A	Harzburgite (protomylonite)	84%	9%	1%	3%	3%	<1%	1346	435	96	558	0.28	154	1.69	1.74	1.6	0.63	0.66	1.4	#	2.0
15-FI-04B	Harzburgite (protomylonite)	70%	12%	1%	4%	13%	<1%	1063	456	402	518	0.36	82	1.76	1.91	1.0	0.43	0.63	1.1	2.2	1.2
15-FI-05	Harzburgite	75%	13%	2%	5%	5%	<1%	2092	943	815	669	0	–	1.99	1.88	1.6	0.66	0.76	1.8	#	4.6
15-FI-08A	Ol–Websterite with dunitic rims	37%	7%	53%	2%	1%	<1%	2310	1391	4963	640	0	–	2.08	1.84	3.4	0.27	0.56	#	3.6	#
15-FI-08B	Lherzolite	74%	12%	10%	1%	3%	<1%	2186	1281	1061	679	0	–	1.94	1.73	2.9	0.12	0.48	3.0	3.9	#
15-FI-09	Wehrlite	58%	2%	38%	2%	0%	<1%	1954	862	1726	1172	0	–	1.65	2.1	2.5	0.17	0.34	#	3.0	#
15-FI-10	Harzburgite	65%	19%	1%	6%	9%	<1%	1716	1001	268	794	<0.01	514	2.38	2.03	1.9	0.57	1.62	1.9	#	6.1
15-FI-11	Harzburgite (protomylonite)	53%	20%	3%	3%	21%	<1%	1623	1328	1565	463	0.03	403	1.97	2.15	1.4	0.50	1.19	1.5	#	4.2
15-FI-12	Harzburgite (protomylonite)	66%	15%	<1%	16%	2%	<1%	1614	688	153	946	0.09	215	2.2	1.6	1.4	0.52	0.43	1.7	6.8	2.4
15-FI-13	Harzburgite	59%	25%	2%	13%	<1%	<1%	1442	912	409	995	0	–	2.2	1.92	1.2	0.49	0.74	1.3	4.8	2.1
15-FI-16	Harzburgite	74%	10%	3%	2%	<1%	1%	2201	872	724	671	0	–	2.02	1.81	2.1	0.20	0.98	2.5	#	#
15-FI-17	Dunite	94%	<1%	<1%	<1%	5%	1%	5064			141	0	–	1.53	1.44	#	#	0.54	#	#	#
15-FI-18	Dunite	97%	<1%	<1%	1%	<1%	1%	4628			526	0	–	1.62	1.6	#	#	0.49	#	#	#
15-FI-19A	Harzburgite	78%	15%	5%	<1%	<1%	1%	2414	1342	1068	196	0	–	*	*	1.9	0.46	0.44	3.1	#	#
15-FI-19C	Harzburgite	78%	7%	<1%	13%	<1%	<1%	2038	1028	344	1063	0	–	*	*	1.6	0.64	0.49	#	#	5.8
15-FI-20A	Harzburgite	82%	11%	<1%	6%	<1%	<1%	2645	1306		1008	0	–	*	*	2.1	0.63	0.45	4.3	#	#
15-FI-20B	Harzburgite	70%	25%	<1%	4%	<1%	<1%	2710	2335	406	1475	0	–	*	*	2.1	0.72	0.50	3.8	#	#
15-FI-20C	Harzburgite with orthopyroxenite layer	63%	29%	1%	3%	4%	<1%	2340	3479	634	1300	0	–	*	*	2.1	0.17	0.47	5.2	#	#
15-FI-20D	Harzburgite with orthopyroxenite layer	56%	41%	<1%	1%	2%	<1%	2051	6065		1532	0	–	*	*	2.5	0.60	0.46	#	#	#
15-FI-21A	Ol–Websterite (protomylonite)	31%	30%	38%	1%	0%	0%	5282	4890	4356	330	0.02	332	*	*	#	#	0.86	3.2	3.8	#
15-FI-21B	Lherzolite	71%	15%	9%	<1%	<1%	4%	2581	1757	2056	220	0	–	*	*	1.8	0.46	0.62	3.0	#	#
15-FI-21C	Harzburgite	83%	10%	1%	5%	<1%	1%	2217	962	596	978	0	–	*	*	2.6	0.52	0.35	2.3	#	4.1
15-FI-21D	Dunite	98%	<1%	<1%	<1%	<1%	1%	3972				0	–	*	*	2.3	0.72	0.42	#	#	#
15-FI-21E	Harzburgite	85%	9%	1%	5%	<1%	<1%	2034	773	328	851	0	–	*	*	1.6	0.40	0.36	3.2	#	4.6
15-FI-22A	Dunite	87%	2%	1%	7%	2%	1%	3786	683	336	1878	0	–	*	*	1.9	0.62	0.89	#	#	#
15-FI-22B	Harzburgite with orthopyroxenite layer	80%	13%	5%	1%	<1%	1%	2795	1401	883	212	0	–	*	*	2.2	0.37	0.81	3.9	5.0	#
15-FI-22C	Harzburgite with orthopyroxenite layer	66%	26%	1%	7%	<1%	<1%	2153	2219	255	792	0	–	*	*	1.9	0.47	0.44	2.1	#	2.7
15-FI-23A	Dunite	97%	2%	<1%	<1%	<1%	<1%	5205				0	–	*	*	#	#	0.33	#	#	#
15-FI-23D	Harzburgite with orthopyroxenite layer	83%	14%	<1%	<1%	0%	2%	3360	2239			0	–	*	*	2.2	0.47	0.27	#	#	#
15-FI-24A	Harzburgite with orthopyroxenite layer	70%	25%	2%	2%	<1%	<1%	2018	1795	775	831	0	–	*	*	2.0	0.34	0.69	3.1	#	#
15-FI-24C	Harzburgite with orthopyroxenite layer	76%	16%	2%	4%	1%	<1%	2117	1507	748	732	0	–	*	*	1.7	0.35	0.65	3.2	#	#
15-FI-24D	Harzburgite with orthopyroxenite layer	56%	16%	2%	23%	2%	<1%	3125	1979	476	3158	0	–	*	*	2.0	0.58	0.94	3.1	#	5.2
15-FI-24E	Harzburgite	83%	9%	2%	5%	<1%	1%	2304	1064	736	877	0	–	*	*	2.3	0.37	0.64	2.6	#	#
15-FI-25C	Harzburgite	83%	16%	<1%	1%	<1%	1%	2003	1318	224	504	0	–	*	*	1.6	0.37	0.63	2.9	#	#
15-FI-31	Harzburgite (protomylonite)	65%	18%	2%	11%	5%	<1%	1264	719	250	792	0.21	129	2.24	1.82	1.3	0.28	0.78	1.5	2.8	1.8

Methods used in the estimation of these parameters from the EBSD data are described in the Supplementary Material Methods section.
[1] Mean (ponderated by area) apparent ($2D$) diameter in μm.
[2] Mean (arithmetic) apparent ($2D$) diameter in μm.
* Drill-core, thin-section not cut in the XZ plane; true aspect ratios could not be estimated.
# J- and BA-indexes are reported only when more than 100 grains were measured.

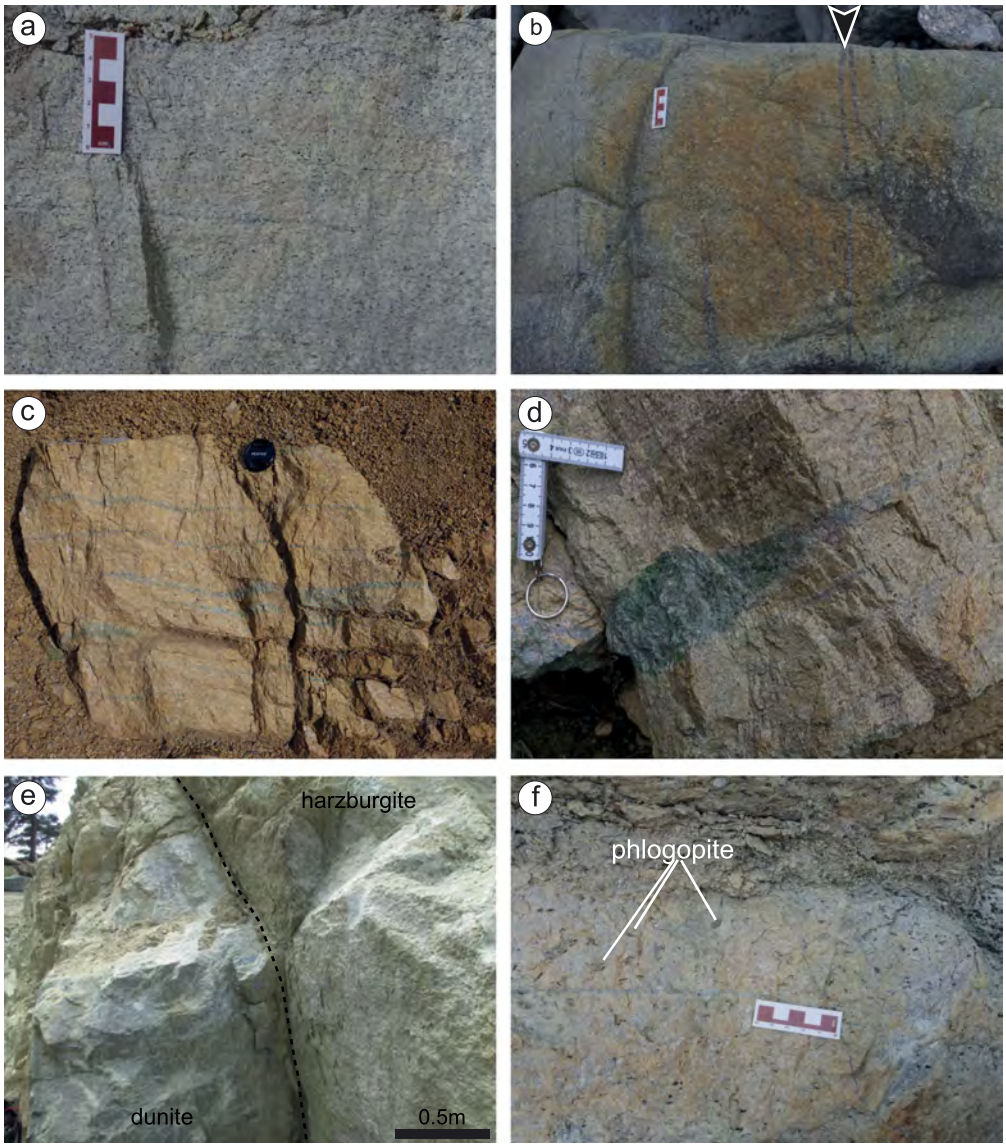

Fig. 2. Macroscopic deformation features. (a) and (b) Harzburgite with a pervasive foliation marked by the shape preferred orientation of pargasite (dark spots in a) parallel to thin orthopyroxenite layers. Arrow in (b) marks the secondary set of orthopyroxenite layers, at ~20° to the one parallel to the foliation in the harzburgite. (c) and (d) Websteritic layers/lenses within harzburgites. The coarse boudinaged websterite layer in (d) shows a characteristic enrichment in orthopyroxene at the contact with the harzburgite. (e) Meter-thick dunitic body within harzburgites. Dunites are commonly more coarse grained than the harzburgites and may contain (f) large flakes of phlogopite.

completely devoid of intragranular misorientation (Fig. 3h), but often, it presents strong undulose extinction and closely-spaced subgrain boundaries (Fig. 3d). The variations in intragranular deformation may be quantified by measurements of the intragranular misorientations, such as the Kernel Average Misorientation (KAM, Fig. 4b and Table 1; cf. definition in the Methods section in the Supplementary Material). There is a relation between the distance to a shear zone and the intragranular deformation of olivine, but closely spaced subgrains in olivine are sometimes observed far from any shear zone. Outside the shear zones olivine grain boundaries are generally straight to gently curved, but the transition between the coarse-grained to the protomylonitic microstructure is gradational; some coarse-grained peridotites show sutured olivine grain boundaries.

Orthopyroxene either defines diffuse layers or occurs dispersed in the harzburgite (Fig. 3a–f). Except in the coarse websterite layers, which have a granular texture, orthopyroxene has very irregular shapes, interstitial-like, with cusp-like terminations at opx–ol–ol triple junctions (Fig. 3a–f). Grain sizes are extremely variable, from 50 μm (interstitial orthopyroxenes forming diffuse bands along olivine grain boundaries) to 1 cm (coarse websterite layer, Table 1). Coarse orthopyroxene crystals often show kinks or undulose extinction (Fig. 3d).

Pargasite is dispersed through the harzburgite, but it may be enriched locally in diffuse elongated lenses or layers. It occurs either as subautomorphic crystals (Fig. 3a–b) or as irregularly shaped crystals with interpenetrating contacts with olivine. The crystals tend to be flattened in the foliation plane and slightly elongated parallel to the lineation (aspect ratios of 1.8 in average, Table 1). Intragranular misorientation in pargasite is rare and, when present, very weak. Grain sizes are in average around 800 μm, but may vary from 140 μm to 3.2 mm (Table 1).

Clinopyroxene occurs as a minor constituent of both harzburgites and dunites, where it is usually dispersed, and as a major constituent of the lherzolites and websterite layers. Clinopyroxene contents tend to be inversely proportional to the pargasite ones. Locally, clinopyroxene rims pargasite crystals (Supplementary Material Fig. S1). Clinopyroxene crystals have very irregular, interstitial-like shapes. Grain sizes are highly variable (100 μm–5 mm), both within a sample and among different sam-

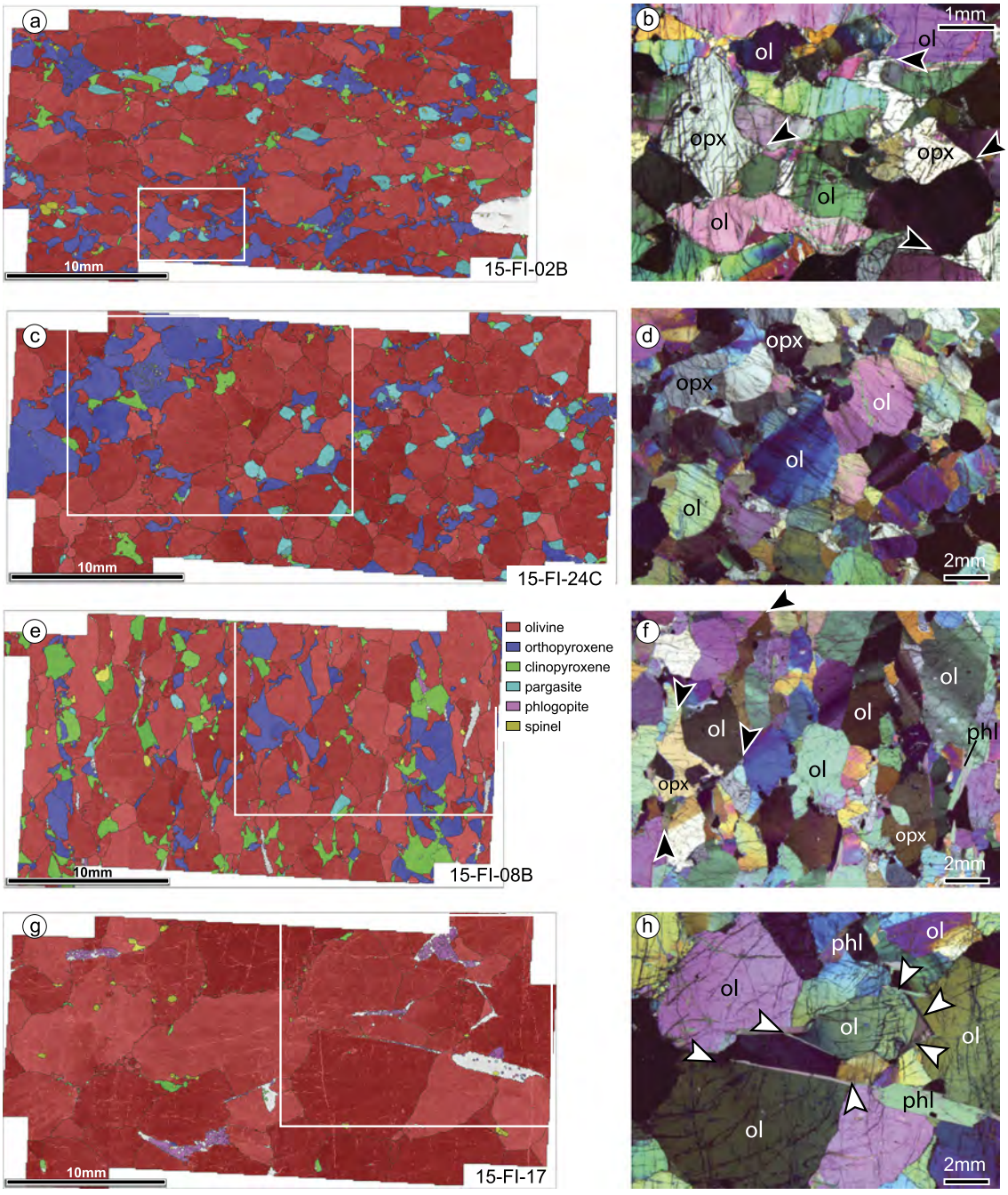

Fig. 3. Microstructures in the coarse-grained peridotites. (a), (c), (e) and (g): EBSD maps illustrating the phases' distribution and shapes. Poorly indexed mineral in (e) and (g) is phlogopite. White boxes locate the photomicrographs in plane-polarized light (b), (d), (f) and (h), which illustrate details of the microstructure, such as the shape-preferred orientation of olivine (ol) in (b) and (f), the irregular shapes and cusp-like terminations of orthopyroxenes (opx), marked by arrows in (b) and (f), widely-spaced subgrain boundaries in olivine in (d), deformation bands and polygonal boundaries of olivine in (d) and (f), or pining of olivine grain boundaries at the contact with phlogopite in (h, white arrows). (For interpretation of the colors in this figure, the reader is referred to the web version of this article.)

ples. Coarse crystals have undulose extinction, indicating variations in crystallographic orientation within the grain.

Phlogopite usually occurs as large flakes, up to 5 mm long, aligned in the foliation (Fig. 3h). Phlogopite content is highly variable. It is usually <5 vol.%, but may attain locally up to 21 vol.%. Phlogopite crystals are often bent and/or display kinks. In all lithologies, but particularly in the dunites, straight olivine grain boundaries butt against large phlogopite flakes (Fig. 3h).

The protomylonites are characterized by a pronounced shape-preferred orientation of lens-shaped olivine crystals (Fig. 5a–d). These crystals show closely spaced subgrain boundaries at high angle to their elongation and are surrounded by a fine-grained matrix (core and mantle structure, Fig. 5a–d). The high density of subgrains and the serrated boundaries of the olivine porphyroclasts indicate that this fine-grained matrix formed essentially by dynamic recrystallization of olivine via an association of bulging and subgrain rotation. Recrystallized area fractions range from <1–36% and recrystallized grain sizes from 80–515 μm (Table 1). Locally, the fine-grained matrix also contains an anastomosed network of ortho- and clinopyroxene-rich seams (Fig. 5c, d), composed by small crystals with interstitial-like shapes. Pyroxene porphyroclasts have irregular shapes and highly indented grain boundaries with embayments filled by olivine. Pargasite and phlogopite show undulose extinction, but are not recrystallized (Fig. 5c, d).

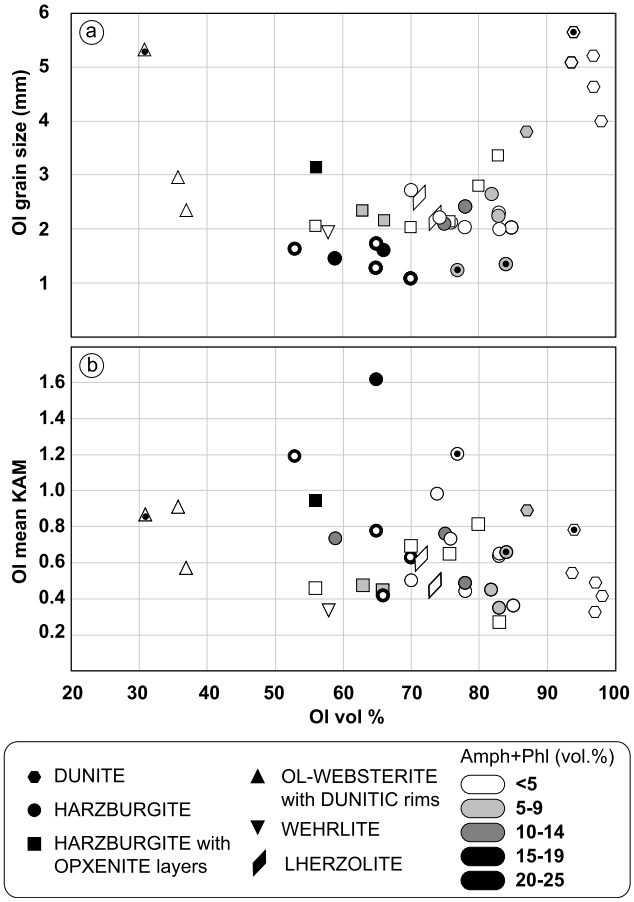

Fig. 4. Olivine modal content (area %) vs. (a) mean area-weighted olivine grain size and (b) mean intragranular misorientation, quantified by the mean (over the entire EBSD map) Kernel Average Misorientation (KAM), which is the misorientation of each pixel relative to the orientation of its nearest neighbors within the grain. Symbols indicate the rock type and the grey filling, the modal abundance of pargasite + phlogopite. Dotted symbols indicate protomylonites.

5. Crystal preferred orientations

Representative crystal preferred orientations (CPO) of olivine, orthopyroxene, pargasite, clinopyroxene, and phlogopite in the Finero Mantle peridotites are displayed in Fig. 6. Data acquisition and treatment methods, as well as CPO data for all samples, are presented as Supplementary Material (Methods and Fig. S2). A characteristic feature of the Finero peridotites is the low strength of olivine CPO patterns, which is evidenced by comparing olivine J-index in Finero peridotites to data from other peridotite massifs and xenoliths (Fig. 7). In contrast, when present in concentrations >1%, pargasite systematically displays a clear CPO. In most cases, pyroxenes show weak, but clear CPO. Both pargasite and orthopyroxene CPO are characterized by a [001] maximum in the foliation plane, which defines the lineation (Fig. 6). Protomylonites display olivine, pargasite, ortho- and clinopyroxene CPO similar in both strength and patterns to those of the coarse-grained peridotites outside the shear zones (Figs. 6 and 7).

Olivine displays a wide range of CPO patterns. Most samples display an axial-[010] CPO characterized by a weak concentration (≤3 multiples of a uniform distribution, m.u.d) of [010] normal or at high angle to the foliation, while [100] and [001] form wide girdles sub-parallel to the foliation marked by the olivine and pargasite SPO (Figs. 6 and 7). In more than half of these samples, [100] forms a weak maximum subparallel to the lineation defined by the pargasite and orthopyroxene [001] maxima, but other samples show either [001] aligned in the lineation, no clear maxima of [100] and [001], or weak maxima of both axes parallel to the lineation. Weak orthorhombic olivine CPO are also observed (Figs. 6 and 7); they tend to display weak concentrations of [010] normal to the foliation and of [100] parallel to pargasite and orthopyroxene [001] maxima. In rare cases, olivine displays orthorhombic CPO patterns oblique to the foliation and the other minerals CPO. A few samples display almost random olivine CPO. With the exception of clinopyroxene-rich peridotites, which show slightly stronger axial-[010] olivine CPO (maximum concentration ≥5 m.u.d.), there is no simple relation between modal composition and olivine CPO type or intensity (Fig. 7). Dunites display olivine CPO similar to the harzburgites' ones, but its analysis is hindered because it can be compared to neither a SPO nor the CPO of other phases.

Pargasite CPO is characterized by a concentration of [100] normal to the foliation marked by the olivine SPO and to the compositional banding. [001] tends to form a girdle in the foliation plane, with a maximum that defines the lineation. The intensity of this maximum varies among the samples, but it is usually weaker than the [100] maximum concentration. [010] is more dispersed.

Orthopyroxene CPO is more dispersed, but usually similar to the pargasite one. Rare samples, like harzburgite 15-FI-16 in Fig. 6, display orthopyroxene CPO oblique to the olivine SPO.

Clinopyroxene, when present in large amounts, as in olivine–websterite 15-FI-2A and wehrlite 15-FI-9 (Supplementary Material Fig. S2), shows a clear CPO marked by a concentration of [010] normal to the foliation and a girdle distribution of [001] in the foliation plane with a maximum parallel to the pargasite and orthopyroxene [001] maxima. When present as a minor phase, the clinopyroxene CPO is usually similar to the orthopyroxene and pargasite ones, but more dispersed.

Phlogopite, when present, displays a strong concentration of [001] normal to the foliation and girdle distributions of [100] and [010] in the foliation plane.

6. Hydroxyl content in olivine and pyroxenes

Hydrous defects speciation and concentration in olivine and pyroxenes from representative samples covering the diversity of olivine CPO were analyzed by means of infrared spectroscopy in double polished thick sections (micro-FTIR, sample thickness 340–360 µm, cf. Supplementary Material for details in the data acquisition and treatment methods).

Olivine is characterized by very low hydroxyl content grouped into two frequency ranges (Fig. 8). Peaks related to titanoclinohumite point defects (3572 and 3523 cm^{-1}) dominate the high frequency range, which also shows subsidiary peaks related to hydroxylated Si-vacancies (3584, 3564, 3542 and 3480 cm^{-1}, e.g. Berry et al., 2005; Padrón-Navarta et al., 2014). Water content associated with the high-frequency bands spans 2–3 ppm wt. of equivalent H_2O (30–50 $H/10^6Si$, Table 2, using Bell et al., 2003 calibration; using the most recent calibration of Withers et al., 2012 the range is reduced to 1–2 ppm wt. H_2O). Half of the analyzed samples show in addition a broad band centered on 3240 cm^{-1}, which is attributed to hydroxylated magnesium vacancies (Berry et al., 2005; Lemaire et al., 2004). This band contributes with 1–2 ppm wt. H_2O. A diffuse band located at 3400 cm^{-1} observed in two samples (15-FI-21A, cf. Fig. 8, and 15-FI-31) might correspond to minute titanoclinohumite lamellae (Hermann et al., 2007; Shen et al., 2014). Total contents are <4 ppm wt. of equivalent H_2O (Table 2).

The infrared spectra of orthopyroxene are systematically dominated by a band centered at 3414 cm^{-1} (Fig. 8). This is unusual for mantle orthopyroxenes, which spectra are almost always dominated by a band at 3590 cm^{-1} (Mosenfelder and Rossman, 2013; Demouchy and Bolfan-Casanova, 2016). Water content in orthopyroxene is rather low (97–124 ppm wt. H_2O, Table 2) comparatively

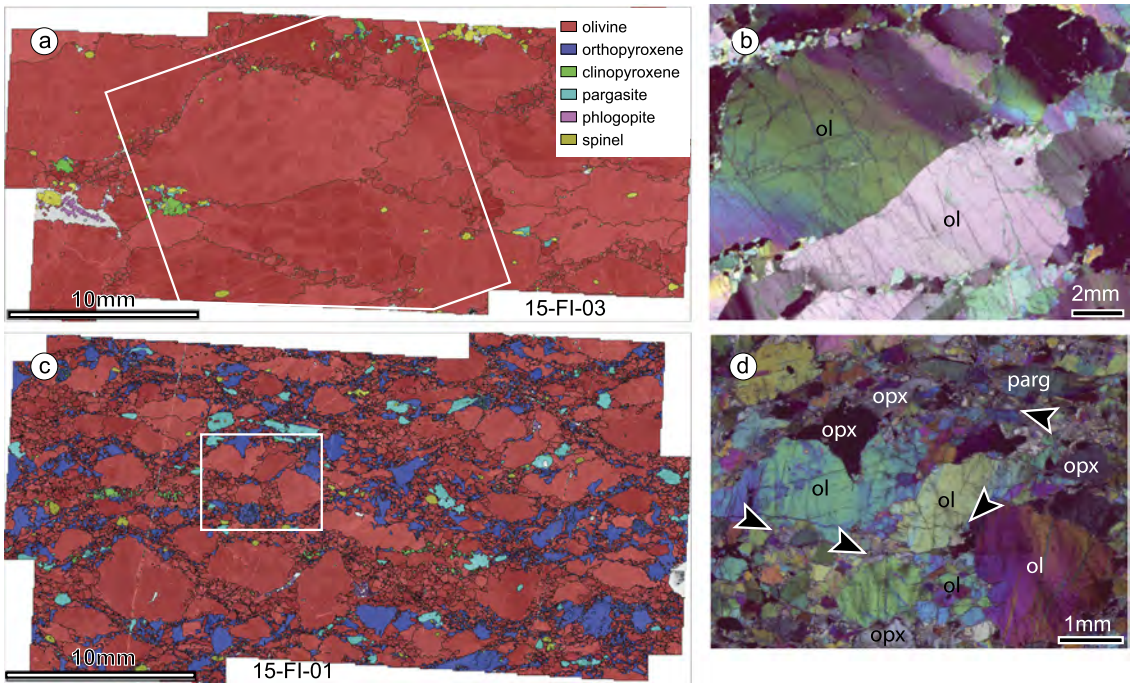

Fig. 5. Microstructures in the protomylonites. (a) and (c): EBSD phase maps illustrating the phases' distribution and shapes. Note the irregular shape of pyroxenes and the fine-grained orthopyroxene-rich seams surrounding coarse lens-shape olivine crystals in (c). Poorly indexed mineral in (a) is phlogopite. White boxes locate the photomicrographs (b) and (d) showing details of the microstructures, such as deformation bands and undulose extinction in coarse lens-shaped olivine surrounded by a fine-grained matrix composed by olivine (b) or olivine and orthopyroxene (arrows in d). Pargasite occurs as flat subhedral grains without evidence of recrystallization (c, d). (For interpretation of the colors in this figure, the reader is referred to the web version of this article.)

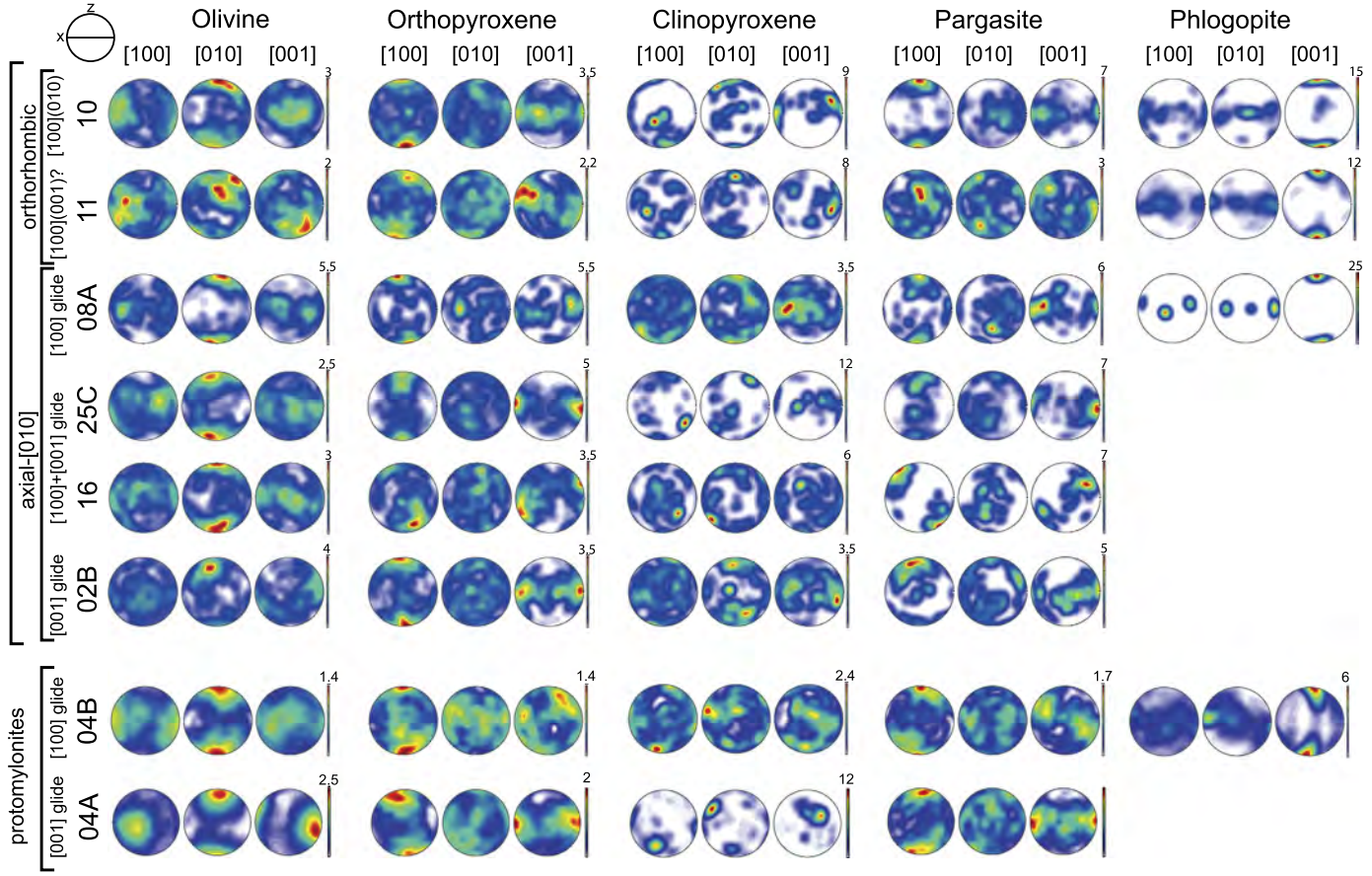

Fig. 6. Pole figures (stereographic projection, lower hemisphere) illustrating the diversity of crystal preferred orientations of olivine, pyroxenes, pargasite, and phlogopite in the Finero peridotites. Insert on the top left indicates the orientation of the structural reference frame. Values at the top of scale bars indicate the maximum concentration in multiples of uniform distribution units.

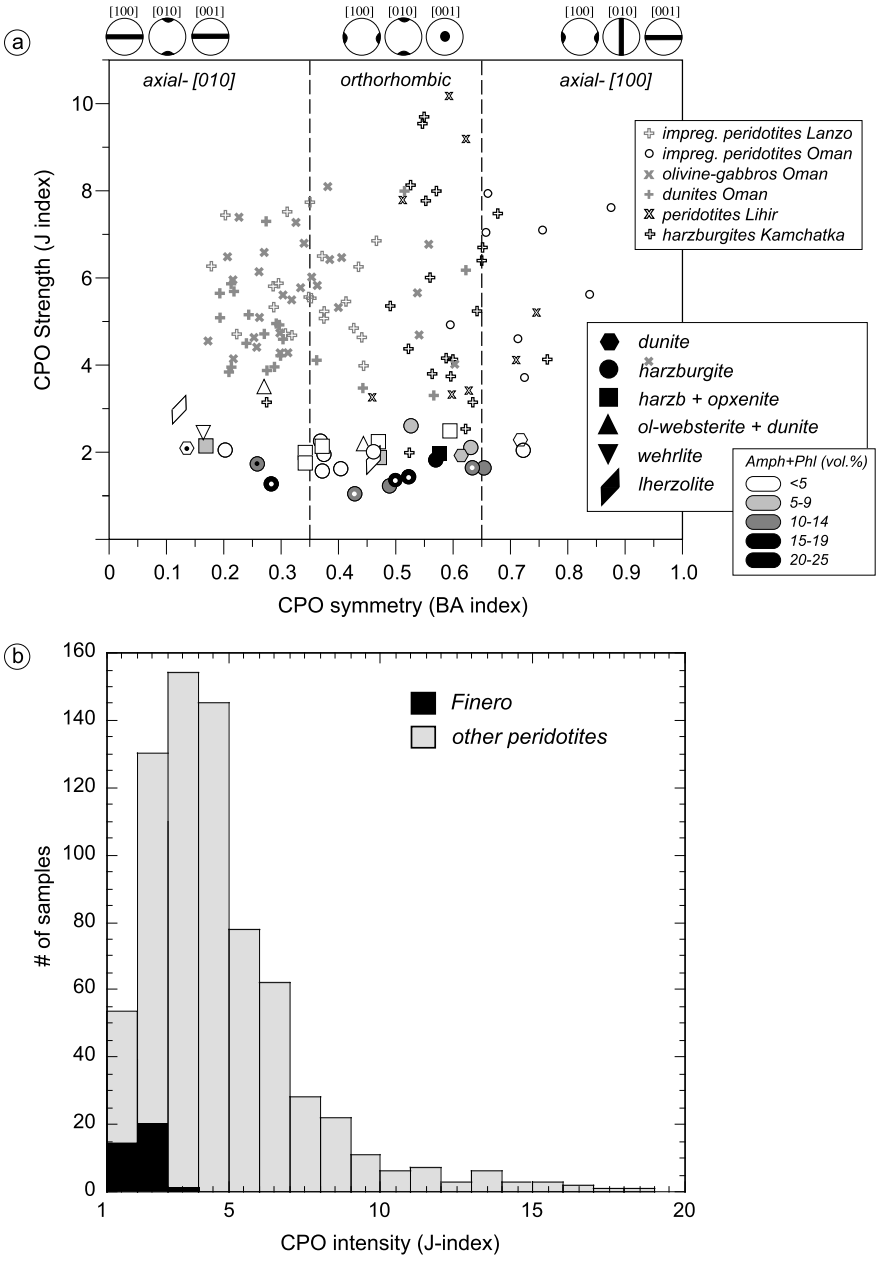

Fig. 7. Olivine crystal preferred orientations (a) J-index *vs.* BA-Index, (b) J-index distribution of the Finero peridotites relative to global J-index database (Tommasi and Vauchez, 2015). Dotted symbols in (a) indicate protomylonites.

Table 2
Water content associated with hydrous point defects obtained by FTIR for some representative samples.

Sample	Lithology	Thickness (μm)	C_{OH} olivine[1] (ppm wt.)		C_{OH} opx[2] (ppm wt.)	C_{OH} cpx[2] (ppm wt.)	$Kd^{opx/ol*}$	$Kd^{cpx/opx}$
			[Ti] + [Si]	[Mg]				
15-FI-8B	Coarse-grained lherzolite	339	3.2	0.4	111	267	30	2.4
15-FI-17	Coarse-grained dunite	361	1.7	–	–	–	–	–
15-FI-21A	Coarse-grained ol–websterite	347	3.1	0.8	124	233	32	1.9
15-FI-24C	Coarse-grained harzburgite	351	1.9	0.2	98	–	47	–
15-FI-31	Harzburgite (protomylonitic)	349	2.0	1.6	97	–	27	–

[1] Water content in olivine using Bell et al. (2003) calibration. Integration ranges: high frequency (titanium-clinohumite point defects [Ti] and Si vacancies [Si]): 3589–3448 cm^{-1} and low frequency (hydrated magnesium vacancies [Mg]): 3314–3096 cm^{-1}.

[2] Integration range for Opx: 3750–2850 cm^{-1} and for Cpx: 3750–3100 cm^{-1}. Calibrations from Bell et al. (1995).

* Only the high frequency group in olivine is included in the Kd calculation.

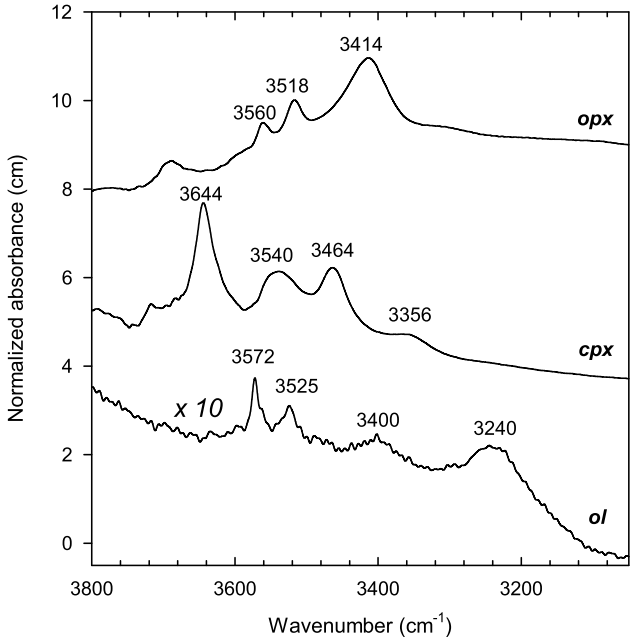

Fig. 8. Representative thickness-normalized infrared spectra (average unpolarized measurements) for olivine and pyroxenes from a coarse-grained peridotite (15-FI-21A). Olivine spectrum is multiplied by a factor of 10 for clarity. Spectra are not baseline corrected and the crystals are mostly free of hydrous inclusions.

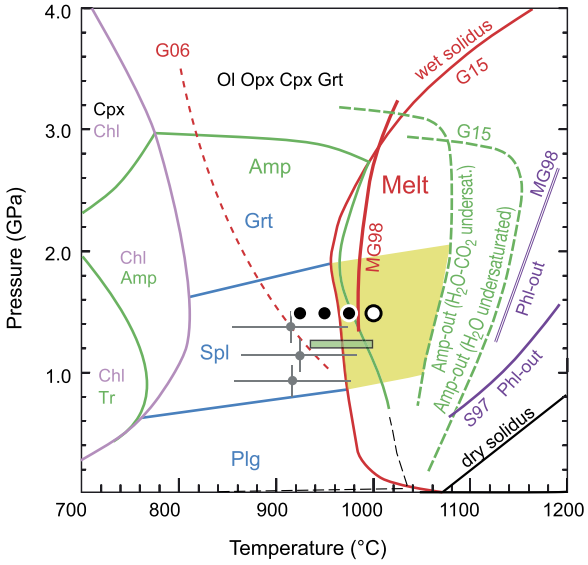

Fig. 9. Temperature–pressure phase diagram showing the main reactions constraining the conditions for the deformation producing the pervasive foliation of the coarse-grained Finero peridotites (yellow field). Continuous and dashed green lines bound the pargasite (Amp) stability field under H_2O-saturated, H_2O–CO_2-undersaturated, and H_2O-understaturated conditions, respectively (Green, 2015 and references therein). Stability limits for phlogopite (Phl) in equilibrium with enstatite are MG98: Mengel and Green (1989) and S97: Sato et al. (1997). Wet solidus curves (in red) are G15: Green (2015, H_2O-saturated), MG98: Mengel and Green (1989), and G06: Grove et al. (2006). Black and white circles indicate experimental data on a model metasomatized peridotite from Mengel and Green (1989): white circles indicate assemblages composed by hydrous melt + amphibole + phlogopite (+ olivine, ortho- and clinopyroxene, spinel) and black ones, aqueous fluid + amphibole + phlogopite (+ olivine, ortho- and clinopyroxene, spinel). For comparison, conventional geothermobarometry data for Finero peridotites (green box, Ernst, 1978) and for the Internal Gabbro Unit (gray circles, A. Langone, unpublished data based on the Cpx–Opx geothermometer of Wood and Banno, 1973 and on the Grt–Opx geobarometer of Harley and Green, 1982) are also displayed. (For interpretation of the references to color in this figure legend, the reader is referred to the web version of this article.)

to usual mantle peridotite values (Demouchy and Bolfan-Casanova, 2016).

Clinopyroxene spectra are dominated by the band centered at 3644 cm^{-1}, as usually in mantle clinopyroxenes (Demouchy and Bolfan-Casanova, 2016), but the contribution of lower frequency bands is remarkable (Fig. 8). Water content in clinopyroxene ranges between 233–267 ppm wt. H_2O (Table 2). This implies water partitioning (Kd) between clino- and orthopyroxene of 1.9–2.4.

In contrast to olivine and pyroxenes, which display rather low concentrations of hydroxylated defaults, amphibole and phlogopite show near stoichiometric water contents. SIMS analyses performed at IGG-CNR in amphibole and phlogopite from a harzburgite, according to the procedure described by Ottolini et al. (1995), give H_2O contents of 1.93 ± 0.05 wt.% and 4.3 ± 0.2 wt.%, respectively.

7. Discussion

7.1. Deformation in presence of hydrous melts

Previous geochemical studies indicate that the ubiquitous enrichment in pargasite and phlogopite and the pyroxenite layering in the Finero Mantle Peridotite unit result from reactive percolation of hydrous silica-rich melts (e.g., Zanetti et al., 1999, 2016; Morishita et al., 2008). The present study constrains that this percolation is concomitant with the high-temperature deformation, which produced the pervasive tectonic fabric in the massif. Multiple observations support this interpretation:

- websterite and orthopyroxenite layers are systematically parallel to the foliation, but show diffuse contacts with the peridotite, which imply that this parallelism cannot be explained by tectonic transposition;
- pargasite and phlogopite have strong shape and crystal preferred orientations, which are consistent with the olivine shape preferred orientation, but display subhedral or interstitial-like shapes and very weak intracrystalline deformation. This suggests oriented crystallization and growth in a deviatoric stress field consistent with the one that produced the pervasive foliation and lineation;
- orthopyroxene and clinopyroxene in the peridotite exhibit interstitial-like shapes, but clear crystal preferred orientations, which are coherent with the CPO of the hydrous minerals and with the SPO of olivine and pargasite. This also suggests synkinematic growth.

Altogether, these observations imply that the pervasive deformation of the Finero Mantle Peridotite unit occurred at pressure and temperature conditions under which pargasite, phlogopite, spinel, and a hydrous melt were stable (Fig. 9). The maximum pressure is constrained by the stability of pargasite ($P < 2.8$ GPa) and by the occurrence of spinel ($P < 2.0$ GPa) in experiments performed in systems with major element compositions appropriated to the study of metasomatized peridotites, such as the Finero peridotites (Mengel and Green, 1989; Green et al., 2014). Maximum temperature conditions are constrained by the stability of pargasite. Maximum values (up to 1130 °C at 1.5 GPa) are obtained for a H_2O undersaturated system (Fig. 9). The upper limit of the stability field of pargasite + melt is displaced to lower temperatures if CO_2 is present in the system (1050–1080 °C at 1.5 GPa in a system saturated or under-saturated in a H_2O–CO_2 fluid, Fig. 9; Green, 2015). Primary graphite intergrowths in phlogopite from harzburgites imply that the Finero melts contained both H_2O and CO_2 (Ferraris et al., 2004). If water-saturated conditions were present, the assemblage pargasite + phlogopite + hydrous melt tightly constrains the temperature of deformation at 980–1000 °C at 1.5–2.0 GPa (Fig. 9).

The high modal proportion of hydrous minerals and near stoichiometric water contents of pargasite suggest indeed conditions close to saturation in the Finero Mantle Peridotite unit, implying that the temperature conditions for the pervasive deformation were close to this lower bound. It is noteworthy that, if the Grove et al. (2006) wet peridotite solidus (G06, Fig. 9) is considered, the lower temperature limit is substantially decreased (down to 880 °C at 1.8 GPa, Fig. 9). However, the validity of this wet solidus is debated (Green et al., 2014).

Upper bounds of conventional thermometry data on the Finero Mantle Peridotite (1000–1060 °C, Fig. 9) are consistent with the conditions for the pervasive deformation of the Finero Peridotite determined based on the petrological assemblage (980–1080 °C). Conventional geothermobarometry data on the garnet-bearing gabbros in contact with the Finero Mantle Peridotite unit (∼920 ± 60 °C and ∼0.8–1.4 GPa, Fig. 9), which show a magmatic foliation parallel to the pervasive foliation of the peridotite, further constrain the lower bound for the conditions of deformation of the peridotite, since these data record the cooling of the gabbros after solidification, that is, the conditions that followed the development of the pervasive foliation of the peridotite. Finally, the presence of sapphirine in gabbro veins that crosscut the peridotite suggests residence of the Finero complex at pressures ≥1.1 GPa up to Mesozoic times (Giovanardi et al., 2013).

7.2. Deformation processes and mantle rheology in presence of hydrous melts

Microstructures in the Finero Mantle Peridotite are characteristic of deformation at low stress conditions. All minerals have very coarse grain sizes and there is no evidence for grain size reduction due to dynamic recrystallization, despite the well developed pervasive foliation and layering that characterize the massif, which imply non-negligible finite strains.

In mantle rocks, olivine, as the main volumetric phase, accommodates most of the deformation and controls the rheological behavior. The olivine microstructure and crystal preferred orientations are therefore reliable markers of the deformation processes and indicators of the physical conditions at which the deformation occurred. The olivine microstructure and crystal preferred orientations in the Finero Mantle Peridotite are peculiar. Olivine occurs as elongated grains with a clear shape preferred orientation (Fig. 3, Table 1) but, when it is not affected by the late deformation that formed the shear zones, it displays very low densities of intragranular deformation features (undulose extinction, subgrains, Fig. 3). Moreover, olivine crystal preferred orientations are extremely weak (Figs. 6 and 7). The present study also highlights abundant evidence for grain growth of olivine, which is only blocked by pinning, leading to grain sizes up to 5 mm (Figs. 3 and 4).

Two scenarios might explain these observations. The first one is to suppose that static grain growth completely erased the olivine intracrystalline deformation features and changed the CPO. However, this would imply grain boundary migration over distances >mm and, hence, in abnormally fast grain growth for the temperatures inferred for this system (<1080 °C). The presence of fluids and melts in the intergranular space may accelerate grain growth (Karato, 1989; German and Olevsky, 1998; Faul and Scott, 2006), but there is no evidence of static crystallization of randomly oriented hydrous phases, suggesting that crystallization of hydrous phases did not outlast deformation. The alternative hypothesis is that the observed microstructures and CPO record the deformation processes at play and that percolation of hydrous melts, not only favored grain growth, but also contributed to the deformation via stress-controlled dissolution and precipitation and advective transport of matter by the melts. The hydrous nature of the melts should improve the efficiency of this process, since introduction of water in a melt enhances cation diffusion rates (Zhang et al., 2010 and references therein), decreases the melt viscosity (Richet et al., 1996; Whittington et al., 2000; Giordano and Dingwell, 2003; Robert et al., 2013) and, by consequence, increases the transport rates by advection. Preferential growth on extensional sites might explain the shape-preferred orientation of olivine, pargasite, and, although less clear because of the more irregular shapes, of pyroxenes (Figs. 3 and 5). Presence of low-viscosity melt films along grain boundaries may also favor sliding, which will contribute to dispersion of the CPO.

The strong pargasite and phlogopite CPO, together with their subhedral or interstitial shapes and weak intracrystalline deformation, point to oriented crystallization and growth. The physical parameters controlling this oriented growth are nevertheless still poorly constrained. Two hypotheses may be proposed: (i) anisotropic growth controlled by the evolution of the shape of the melt-filled pores in a deforming rock and (ii) preferential nucleation and growth of crystals in orientations that lead to a decrease in the local elastic energy of the system.

Olivine CPO patterns are not only weak, but highly variable. The interpretation of these patterns in terms of deformation by dislocation creep would imply that the dominant glide system of olivine changes, sometimes within a few meters, from the 'dry', low stress [100](010) system to the 'wet' and high stress [001](100) and [001](010) systems. FTIR measurements indicate nevertheless that olivine crystals are systematically dry (<4 ppm wt.; Table 2). Interpretation of the measured hydrous point defect content in olivine as primary ones, not modified by hydrogen loss at later stages in the evolution of the massif, is justified by the very low diffusivity of hydrogen in Si-vacancies, either as pure hydroxylated Si-vacancies or as complex defects associated to titanium (Padrón-Navarta et al., 2014), which are the most common hydrous point defects in olivine in the Finero peridotites (Fig. 8). One cannot discard the possibility of some post-deformation hydrogen loss due to diffusion of the hydrogen stored in octahedral M-type defects, which have higher diffusivities. Ab initio calculations as well as experimental data (Berry et al., 2005; Walker et al., 2007; Padrón-Navarta and Hermann, submitted for publication) suggest, however, that hydroxylated M-vacancies play a subordinated role in the "water" solubility in olivine at low pressure. The maximum primary hydrous point defect content in olivine may be estimated to be ≤35 ppm wt. H_2O based on (1) the pressure and temperature conditions of Finero, and (2) the "water" solubility in olivine under such conditions (Padrón-Navarta and Hermann, submitted for publication). This value corresponds to water saturated conditions and would be lowered as a function of the water activity conditions prevailing during the metasomatic event. Yet, even this maximum estimation is already lower than the values at which the transition between [100](010) and [001](100) glide is observed in Jung et al. (2006) experiments.

Changes in olivine CPO symmetry might be related to fluctuations in the composition of the fluids in the system. Previous studies on peridotites deformed in presence of water-poor basaltic melts (Oman and Lanzo; Higgie and Tommasi, 2012, 2014; Murray Ridge: Tommasi et al., 2006) or of aqueous fluids (Kamchatka and Lihir; Soustelle et al., 2010, 2013) show indeed different olivine CPO patterns as a function of the fluid composition and of the associated reactions. Axial-[010] patterns predominate when deformation is associated with refertilization reactions due to interactions with basaltic melts, whereas axial-[100] or orthorhombic patterns predominate when deformation occurs in presence of aqueous fluids or when it is associated with dunitization reactions (Fig. 7a). The olivine CPO data in the Finero Mantle Peridotite covers the entire range of symmetries observed in other peridotites deformed in presence of melts or fluids. However, the variations in CPO patterns in the Finero Mantle Peridotite cannot be simply

related to changes in the modal composition (Fig. 7a). The only exceptions are the clinopyroxene-rich peridotites, which have in average stronger olivine CPO (Figs. 6 and 7a). Their low pargasite content and the presence of clinopyroxene rims on pargasite point to a local decrease in water content in the melt. This suggests that a decrease in the water content in the melt might result in a larger contribution of dislocation creep to deformation.

Which are the stress conditions prevailing during this deformation? The coarse grain sizes imply that stresses were low during the initial pervasive deformation episode. Even for the part of the deformation accommodated by dislocation creep, easy grain boundary migration was effective in avoiding hardening due to dislocations pinning. However, the strong contribution of fluid-assisted transport processes to deformation and the effective grain boundary migration, which probably continued under static conditions, hinder any stress quantification.

7.3. The evolution from distributed to localized deformation

The formation of protomylonites records a marked change in deformation mode: from homogeneously distributed to localized. The shear zones have a complex evolution, with some that were likely reactivated more than once, with the last episodes at the brittle–ductile transition (Brodie, 1980, 1981; Altenberger, 1995; Matysiak and Trepmann, 2015). However, the protomylonites that compose their external domains have preserved the traces of the first stages of strain localization.

The analysis of their microstructure highlights a change in deformation processes. The closely-spaced subgrain boundaries and the grain size reduction by dynamic recrystallization of olivine (Fig. 5) indicate deformation by dislocation creep under higher work rates than those prevailing during the homogeneous deformation episode. Stresses calculated based on the measured mean recrystallized grain sizes (80–515 µm, Table 1) using the piezometers of Karato et al. (1980) and Van der Wal et al. (1993) range between 9 and 43 MPa. These stresses constitute an upper bound for those involved in the formation of the pervasive coarse grained foliation, which must have been lower than 10 MPa.

The fact that closely-spaced subgrain boundaries in olivine are observed even at significant distance from the shear zones suggests that the entire massif was submitted to the high stress event, but that the associated deformation was heterogeneous, progressively localizing into shear zones. It is noteworthy that the localized deformation does not affect preferentially the hydrous phases, which show evidence for intracrystalline deformation, but are not recrystallized (Fig. 5). Fine-grained domains are composed solely by olivine, formed at the expenses of the coarse grains by dynamic recrystallization by bulging and subgrain rotation, and by seams of ortho- and clinopyroxenes with interstitial shapes.

The change in deformation processes and in the repartition of the deformation (localized instead of pervasively distributed) implies a change in the physical environment leading to an increase in strength of the peridotites. Two scenarios may be envisaged: either two deformation episodes spaced in time or a continuous deformation under decreasing temperature conditions, where the transition between melt-present to melt-absent conditions resulted in a change in the rheological behavior. Foliations in the protomylonites are subparallel to those of the low-stress pervasive deformation, implying similar kinematics. Based on this observation, we favor the second scenario, because for explaining similar kinematics between two events separated in time, we need to invoke reactivation of the fabric produced by the first deformation. However, there are no obvious physical reasons for such reactivation. The olivine CPO is weak and, hence, the CPO-induced mechanical anisotropy is low (Tommasi et al., 2009), no grain size reduction is associated with the pervasive deformation, and the presence of oriented hydrous phases does not seem to result in weakening, since there is no spatial relation between hydrous phase contents and strain localization.

Similarly to Hidas et al. (2016), we interpret the seams of fine-grained pyroxenes within the fine-grained matrix of the protomylonites (Fig. 5) as resulting from remobilization by dissolution–crystallization processes, evidencing the presence of fluids during the formation of the protomylonites. A change in the composition of the fluid phase from hydrous melts to aqueous fluids has been observed in experiments in response to a temperature decrease below 1000 °C (cf. Mengel and Green, 1989 data in Fig. 9). It is therefore consistent with cooling of the massif. Analysis of the microstructure of the protomylonites (Fig. 5) indicates that these fluids did not produce remobilization or recrystallization of the pargasite or phlogopite, suggesting equilibrium between these phases and the fluids and, hence, a limited change in temperature. Altogether, these observations favor the hypothesis of a continuous evolution of the system under decreasing temperature conditions and imply that the nature of the fluids present in the system play a major role in controlling its mechanical behavior.

The subsequent evolution of the shear zones is well documented. Previous studies report a marked decrease in recrystallized grain size, which attains a few µm in the ultramylonites, and changes in the modal and mineral composition from the protomylonites to the ultramylonites (including the crystallization of other phyllosilicates such as antigorite), which suggest that localized deformation continued under progressively decreasing temperature conditions and increasing work rates in presence of fluids (Brodie, 1980; Altenberger, 1995). These studies also provide evidence for reactivation of these shear zones under even lower temperature conditions, in the chlorite or antigorite stability fields (Altenberger, 1995), or even under brittle conditions (Matysiak and Trepmann, 2015). Reactivation was probably controlled by grain size contrasts, but there is also evidence for formation of new shear zones and faults, which do not reactivate preexisting ones (Matysiak and Trepmann, 2015).

8. Conclusions

Petrostructural data on the Finero Mantle Peridotite unit indicates that the pervasive foliation, which characterizes the massif, was formed by deformation concomitant with the percolation of hydrous Si-rich melts, which produced hydration of the massif via the crystallization of large amounts of pargasite and phlogopite (up to 25 vol.%). Multiple observations corroborate these interpretations:

- the parallelism between the pyroxenitic layering and the pervasive foliation in the peridotites and the diffuse boundaries of the pyroxenitic layers, which imply syntectonic emplacement of these layers;
- the strong SPO and CPO, but subhedral or interstitial shapes and weak intracrystalline deformation of the hydrous phases, which support syntectonic crystallization;
- the interstitial shapes, but clear CPO of the pyroxenes, which suggest syntectonic growth;
- the very coarse olivine grain sizes, which are correlated to the olivine abundance, pointing to very effective grain growth by grain boundary migration, only limited by pinning;
- the elongated shapes and strong SPO, but low intracrystalline deformation, of olivine as well as its extremely weak and highly variable CPO, which suggest that other processes than dislocation creep contributed to deformation.

Altogether, these observations imply that the pervasive deformation of the Finero Mantle Peridotite unit occurred under pres-

sure and temperature conditions that allowed both the presence of hydrous melts and the crystallization of pargasite in the system; this points to temperatures of 980–1080 °C and pressures <2 GPa. The present petrostructural observations also suggest that the presence of hydrous melts strongly changes the deformation processes in the upper mantle, as it results in accommodation of a significant amount of deformation through stress-controlled dissolution and precipitation and advective transport of matter by the melts. The presence of hydrous melts also favors fast grain boundary migration. By consequence, it produces significant rheological weakening, allowing deformation under low stress (<10 MPa) at temperatures as low as 980–1080 °C.

The hypothesis of rheological weakening controlled by the role of hydrous melts in the deformation is corroborated by the low water contents in olivine measured by FTIR (<4 ppm wt. H_2O), which imply that percolation of hydrous melts in the stability field of pargasite does not produces an increase of the hydrous point defect population in olivine sufficient to modify significantly its mechanical behavior.

Analysis of the microstructures of the protomylonites suggests that a weak decrease in temperature leading to transition from melt-present to melt-free (but aqueous fluid-bearing) conditions results in a marked change in deformation processes. It produces an increased contribution of dislocation creep to the total deformation and, by consequence, an increase in the peridotites strength, despite the preservation of aqueous fluids in the system. This change in deformation behavior results in onset of strain localization. It is noteworthy that strain localization is not correlated to the local abundance in pargasite or phlogopite. This emphasizes that crystallization of pargasite or phlogopite in the upper mantle, even when their concentration reaches >25 vol.%, does not produce rheological weakening.

Although the actual strength of the peridotites cannot be quantified based on the present geological observations, the observed changes in deformation behavior are likely to occur atop subduction zones, leading to strong rheological contrast between domains deforming in presence of hydrous melts and melt-absent ones. Another conclusion, which can be derived from the present data, is that the weakening associated with hydrous melts is a transient one, which ceases at their crystallization or extraction.

Acknowledgements

This work was funded by the program SYSTER of the CNRS "Institut des Sciences de l'Univers" (France), by the project MIUR PRIN 2015 "Geochemical and isotopic budget of highly metasomatized sub-continental mantle in the Africa and Europe geodynamic systems: modern and fossil analogues" (Italy), and by a Short Term Mobility grant (2015; A. Langone) of the CNR (Italy). J.A.P.N. is grateful for funding by the ANR Tremplin project [DeepW]. We thank S. Corvò for carrying out FTIR measurements and two anonymous reviewers for their constructive reviews. C. Nevado and D. Delmas prepared high-quality polished thin sections for EBSD measurements, which were performed with the help of F. Barou at the EBSD-SEM national facility at Géosciences Montpellier.

Appendix A. Supplementary material

Supplementary material related to this article can be found online at http://dx.doi.org/10.1016/j.epsl.2017.08.015.

References

Altenberger, U., 1995. Long-term deformation and fluid-enhanced mass transport in a Variscan peridotite shear zone in the Ivrea Zone, northern Italy: a microtextural, petrological and geochemical study of a reactivated shear zone. Int. J. Earth Sci. 84, 591–606. http://dx.doi.org/10.1007/BF00284523.

Beltrando, M., Stockli, D.F., Decarlis, A., Manatschal, G., 2015. A crustal-scale view at rift localization along the fossil Adriatic margin of the Alpine Tethys preserved in NW Italy. Tectonics 34, 1927–1951. http://dx.doi.org/10.1002/2015TC003973.

Berry, A.J., Hermann, J., O'Neill, H.S., Foran, G.J., 2005. Fingerprinting the water site in mantle olivine. Geology 33, 869–872.

Bell, D.R., Ihinger, P.D., Rossman, G.R., 1995. Quantitative and analysis of trace OH in garnet and pyroxenes. Am. Mineral. 80, 465–474.

Bell, D.R., Rossman, G.R., Maldener, J., Endisch, D., Rauch, F., 2003. Hydroxide in olivine: a quantitative determination of the absolute amount and calibration of the IR spectrum. J. Geophys. Res., Solid Earth 108, 2105. http://dx.doi.org/10.1029/2001JB000679.

Brodie, K.H., 1980. Variations in mineral chemistry across a phlogopite shear zone. J. Struct. Geol. 2, 265–272.

Brodie, K.H., 1981. Variation in amphibole and plagioclase composition with deformation. Tectonophysics 78, 385–402.

Cawthorn, R.G., 1975. The amphibole peridotite–metagabbro complex, Finero, northern Italy. J. Geol. 83, 437–454.

Coltorti, M., Siena, F., 1984. Mantle tectonite and fractionated peridotite at Finero (Italian Western Alps). Neues Jahrb. Mineral. Abh. 149, 225–244.

Demouchy, S., Bolfan-Casanova, N., 2016. Distribution and transport of hydrogen in the lithospheric mantle: a review. Lithos 240, 402–425.

Demouchy, S., Tommasi, A., Barou, F., Mainprice, D., Cordier, P., 2012. Deformation of olivine in torsion under hydrous conditions. Phys. Earth Planet. Inter. 202, 56–70. http://dx.doi.org/10.1016/j.pepi.2012.05.001.

Ernst, W.G., 1978. Petrochemical study of lherzolitic rocks from the Western Alps. J. Petrol. 19, 341–392.

Faul, U.H., Scott, D., 2006. Grain growth in partially molten olivine. Contrib. Mineral. Petrol. 151, 101–111. http://dx.doi.org/10.1007/s00410-005-0048-1.

Faul, U.H., Cline, C.J., David, E.C., Berry, A.J., Jackson, I., 2016. Titanium-hydroxyl defect-controlled rheology of the Earth's upper mantle. Earth Planet. Sci. Lett. 452, 227–237.

Fei, H., Wiedenbeck, M., Yamazaki, D., Katsura, T., 2013. Small effect of water on upper-mantle rheology based on silicon self-diffusion coefficients. Nature 498, 213–215.

Ferraris, C., Grobety, B., Früh-Green, G.L., Wessicken, R., 2004. Intergrowth of graphite within phlogopite from Finero ultramafic complex (Italian Western Alps). Eur. J. Mineral. 16, 899–908.

Fumagalli, P., Klemme, S., 2015. Mineralogy of the Earth: phase transitions and mineralogy of the upper mantle. In: Schubert, G. (Ed.), Treatise on Geophysics, 2nd edition. Elsevier, Oxford, pp. 7–31.

Garuti, G., Friolo, R., 1979. Textural features and olivine fabrics of peridotites from the Ivrea–Verbano Zone (Italian Western Alps). Mem. Sci. Geol. 33, 111–125.

German, R.M., Olevsky, E.A., 1998. Modeling grain growth dependence on the liquid content in liquid-phase-sintered materials. Metall. Mat. Trans. A 29, 3057–3067. http://dx.doi.org/10.1007/s11661-998-0213-z.

Giordano, D., Dingwell, D., 2003. Viscosity of hydrous Etna basalt: implications for Plinian-style basaltic eruptions. Bull. Volcanol. 65, 8–14.

Giovanardi, T., Morishita, T., Zanetti, A., Mazzucchelli, M., Vannucci, R., 2013. Igneous spphirine as a product of melt–peridotite interactions in the Finero phlogopite-peridotite massif, western Italian Alps. Eur. J. Mineral. 25, 17–31.

Giovanardi, T., Mazzucchelli, M., Zanetti, A., Langone, A., Tiepolo, M., Cipriani, A., 2014. Occurrence of phlogopite in the Finero mafic layered complex. Open Geosci. 6 (4), 588–613.

Girard, J., Chen, J., Raterron, P., Holyoke, C.W., 2013. Hydrolytic weakening of olivine at mantle pressure: evidence of [100](010) slip system softening from single-crystal deformation experiments. Phys. Earth Planet. Inter. 216, 12–20.

Green, D.H., 2015. Experimental petrology of peridotites, including effects of water and carbon on melting in the Earth's upper mantle. Phys. Chem. Miner. 42 (2), 95–122. http://dx.doi.org/10.1007/s00269-014-0729-2.

Green, D.H., Hibberson, W.O., Rosenthal, A., Kovács, I., Yaxley, G.M., Falloon, T.J., Brink, F., 2014. Experimental study of the influence of water on melting and phase assemblages in the upper mantle. J. Petrol. 55, 2067–2096.

Grove, T.L., Chatterjee, N., Parman, S.W., Médard, E., 2006. The influence of H_2O on mantle wedge melting. Earth Planet. Sci. Lett. 249 (1–2), 74–89.

Harley, S.L., Green, D.H., 1982. Garnet–orthopyroxene barometry for granulites and peridotites. Nature 300, 697–701.

Hartmann, G., Wedepohl, K.H., 1993. The composition of peridotite tectonites from the Ivrea complex, northern Italy: residues from melt extraction. Geochim. Cosmochim. Acta 57, 1761–1782.

Hermann, J., Gerald, J.D.F., Malaspina, N., Berry, A.J., Scambelluri, M., 2007. OH-bearing planar defects in olivine produced by the breakdown of Ti-rich humite minerals from Dabie Shan (China). Contrib. Mineral. Petrol. 153, 417–428.

Hidas, K., Tommasi, A., Garrido, C.J., Padrón-Navarta, J.A., Mainprice, D., Vauchez, A., Marchesi, C., 2016. Fluid-assisted strain localization in the shallow subcontinental lithospheric mantle. Lithos 262, 636–650. http://dx.doi.org/10.1016/j.lithos.2016.07.038.

Higgie, K., Tommasi, A., 2012. Feedbacks between deformation and melt distribution in the crust–mantle transition zone of the Oman ophiolite. Earth Planet. Sci. Lett. 359, 61–72. http://dx.doi.org/10.1016/j.epsl.2012.10.003.

Higgie, K., Tommasi, A., 2014. Deformation in a partially molten mantle: constraints from plagioclase lherzolites from Lanzo, western Alps. Tectonophysics 615, 167–181. http://dx.doi.org/10.1016/j.tecto.2014.01.007.

Jung, H., Katayama, I., Jinag, Z., Hiraga, T., Karato, S., 2006. Effect of water and stress on the lattice-preferred orientation of olivine. Tectonophysics 421, 1–22.

Karato, S.I., 1989. Grain growth kinetics in olivine aggregates. Tectonophysics 168, 255–273.

Karato, S., Toriumi, M., Fujii, T., 1980. Dynamic recrystallization of olivine single crystals during high temperature creep. Geophys. Res. Lett. 7, 649–652.

Kenkmann, T., Dresen, G., 2002. Dislocation microstructure and phase distribution in a lower crustal shear zone – an example from the Ivrea-Zone, Italy. Int. J. Earth Sci. 91, 445–458. http://dx.doi.org/10.1007/s00531-001-0236-9.

Kruhl, J., Voll, G., 1976. Fabrics and metamorphism from the Monte Rosa Root Zone into the Ivrea Zone near Finero, southern margin of the Alps. Schweiz. Mineral. Petrogr. Mitt. 56, 627–633.

Kruhl, J., Voll, G., 1979. Deformation and metamorphism of the western Finero Complex. Mem. Sci. Geol. 33, 95–104.

Lemaire, C., Kohn, S.C., Brooker, R.A., 2004. The effect of silica activity on the incorporation mechanisms of water in synthetic forsterite: a polarised infrared spectroscopic study. Contrib. Mineral. Petrol. 147, 48–57.

Lensch, G., 1968. Die Ultramafitite der Zone von Ivrea und ihre geologische Interpretation. Schweiz. Mineral. Petrogr. Mitt. 48, 91–102.

Lu, M., Hofmann, A.W., Mazzucchelli, M., Rivalenti, G., 1997. The mafic–ultramafic complex near Finero (Ivrea-Verbano Zone), I: chemistry of MORB-like magmas. Chem. Geol. 140, 207–222.

Matysiak, A.K., Trepmann, C.A., 2015. The deformation record of olivine in mylonitic peridotites from the Finero Complex, Ivrea Zone: separate deformation cycles during exhumation. Tectonics 34, 2514–2533. http://dx.doi.org/10.1002/2015TC003904.

Mei, S., Kohlstedt, D.L., 2000a. Influence of water on plastic deformation of olivine aggregates, 1: diffusion creep regime. J. Geophys. Res. 105, 21457–21469.

Mei, S., Kohlstedt, D.L., 2000b. Influence of water on plastic deformation of olivine aggregates, 2: dislocation creep regime. J. Geophys. Res. 105, 21471–21481.

Mei, S., Bai, W., Hiraga, T., Kohlstedt, D.L., 2002. Influence of melt on the creep behavior of olivine–basalt aggregates under hydrous conditions. Earth Planet. Sci. Lett. 201, 491–507.

Mengel, K., Green, D.H., 1989. Stability of amphibole and phlogopite in metasomatized peridotite under water-saturated and water-undersaturated conditions. In: Kimberlites and Related Rocks. Geological Society of Australia Special Publications, vol. 14, pp. 571–581.

Morishita, T., Hattori, K.H., Terada, K., Matsumoto, T., et al., 2008. Geochemistry of apatite-rich layers in the Finero phlogopite–peridotite massif (Italian Western Alps) and ion microprobe dating of apatite. Chem. Geol. 251, 99–111.

Mosenfelder, J.L., Rossman, G.R., 2013. Analysis of hydrogen and fluorine in pyroxenes, I: orthopyroxene. Am. Mineral. 98, 1026–1041. http://dx.doi.org/10.2138/am.2013.4291.

Ottolini, L., Bottazzi, P., Zanetti, A., Vannucci, R., 1995. Determination of hydrogen in silicates by secondary ion mass spectrometry. Analyst 120, 1309–1313.

Padrón-Navarta, J.A., Hermann, J., O'Neill, H.S.C., 2014. Site-specific hydrogen diffusion rates in forsterite. Earth Planet. Sci. Lett. 392, 100–112.

Padrón-Navarta, J.A., Hermann, J., submitted for publication. A subsolidus water solubility equation for the Earth's upper mantle. J. Geophys. Res.

Richet, P., Lejeune, A.M., Holtz, F., Roux, J., 1996. Water and the viscosity of andesite melts. Chem. Geol. 128, 185–197.

Robert, G., Whittington, A.G., Stechem, A., Behrens, H., 2013. The effect of water on the viscosity of a synthetic calc-alkaline basaltic andesite. Chem. Geol. 346, 135–148.

Rutter, E., Brodie, K., James, T., Burlini, L., 2007. Large-scale folding in the upper part of the Ivrea–Verbano zone, NW Italy. J. Struct. Geol. 29, 1–17. http://dx.doi.org/10.1016/j.jsg.2006.08.013.

Sato, K., Katsura, T., Ito, E., 1997. Phase relations of natural phlogopite with and without enstatite up to 8 GPa: implication for mantle metasomatism. Earth Planet. Sci. Lett. 146 (3), 511–526. http://dx.doi.org/10.1016/S0012-821X(96)00246-4.

Selverstone, J., Sharp, Z.D., 2011. Chlorine isotope evidence for multicomponent mantle metasomatism in the Ivrea Zone. Earth Planet. Sci. Lett. 310, 429–440. http://dx.doi.org/10.1016/j.epsl.2011.08.034.

Shen, T., Hermann, J., Zhang, L., Padrón-Navarta, J., Chen, J., 2014. FTIR spectroscopy of Ti-chondrodite, Ti-clinohumite, and olivine in deeply subducted serpentinites and implications for the deep water cycle. Contrib. Mineral. Petrol. 167, 1–15.

Soustelle, V., Tommasi, A., Demouchy, S., Ionov, D.A., 2010. Deformation and fluid–rock interaction in the supra-subduction mantle: microstructures and water contents in peridotite xenoliths from the Avacha Volcano, Kamchatka. J. Petrol. 51, 363–394. http://dx.doi.org/10.1093/petrology/egp085.

Soustelle, V., Tommasi, A., Demouchy, S., Franz, L., 2013. Melt–rock interactions, deformation, hydration and seismic properties in the sub-arc lithospheric mantle inferred from xenoliths from seamounts near Lihir, Papua New Guinea. Tectonophysics 608, 330–345. http://dx.doi.org/10.1016/j.tecto.2013.09.024.

Tommasi, A., Vauchez, A., 2015. Heterogeneity and anisotropy in the lithospheric mantle. Tectonophysics 661, 11–37. http://dx.doi.org/10.1016/j.tecto.2015.07.026.

Tommasi, A., Vauchez, A., Godard, M., Belley, F., 2006. Deformation and melt transport in a highly depleted peridotite massif from the Canadian Cordillera: implications to seismic anisotropy above subduction zones. Earth Planet. Sci. Lett. 252, 245–259. http://dx.doi.org/10.1016/j.epsl.2006.09.042.

Tommasi, A., Knoll, M., Vauchez, A., Signorelli, J.W., Thoraval, C., Logé, R., 2009. Structural reactivation in plate tectonics controlled by olivine crystal anisotropy. Nat. Geosci. 2 (6), 423–427. http://dx.doi.org/10.1038/NGEO528.

Van der Wal, D., Chopra, P., Drury, M., Gerald, J.F., 1993. Relationships between dynamically recrystallized grain-size and deformation conditions in experimentally deformed olivine rocks. Geophys. Res. Lett. 20, 1479–1482.

Walker, A.M., Hermann, J., Berry, A.J., O'Neill, H., 2007. Three water sites in upper mantle olivine and the role of titanium in the water weakening mechanism. J. Geophys. Res. 112, B05211. http://dx.doi.org/10.1029/2006JB004620.

Whittington, A., Richet, P., Holtz, F., 2000. Water and the viscosity of depolymerized aluminosilicate melts. Geochim. Cosmochim. Acta 64, 3725–3736.

Withers, A.C., Bureau, H., Raepsaet, C., Hirschmann, M.M., 2012. Calibration of infrared spectroscopy by elastic recoil detection analysis of H in synthetic olivine. Chem. Geol. 334, 92–98.

Wolff, R., Dunkl, I., Kiesselbach, G., Wemmer, K., Siegesmund, S., 2012. Thermochronological constraints on the multiphase exhumation history of the Ivrea–Verbano Zone of the Southern Alps. Tectonophysics 579, 104–117. http://dx.doi.org/10.1016/j.tecto.2012.03.019.

Wood, B.J., Banno, S., 1973. Garnet–orthopyroxene and orthopyroxene–clinopyroxene relationships in simple and complex systems. Contrib. Mineral. Petrol. 4, 109–124.

Zanetti, A., Mazzucchelli, M., Rivalenti, G., Vannucci, R., 1999. The Finero phlogopite–peridotite massif: an example of subduction-related metasomatism. Contrib. Mineral. Petrol. 134, 107–122. http://dx.doi.org/10.1007/s004100050472.

Zanetti, A., Mazzucchelli, M., Sinigoi, S., Giovanardi, T., Peressini, G., Fanning, M., 2013. SHRIMP U–Pb zircon Triassic intrusion age of the Finero mafic complex (Ivrea–Verbano Zone, Western Alps) and its geodynamic implications. J. Petrol. 54, 2235–2265.

Zanetti, A., Giovanardi, T., Langone, A., Tiepolo, M., Wu, F-Y., Dallai, L., Mazzucchelli, M., 2016. Origin and age of zircon-bearing chromitite layers from the Finero phlogopite peridotite (Ivrea–Verbano Zone, Western Alps) and geodynamic consequences. Lithos 262, 58–74.

Zhang, Y., Ni, H., Chen, Y., 2010. Diffusion data in silicate melts. Rev. Mineral. Geochem. 72, 311–408.